An Offline Parameter Self-Learning Method Considering Inverter Nonlinearity With Zero-Axis Voltage

Qiwei Wang, Nannan Zhao, *Member, IEEE*, Gaolin Wang, *Senior Member, IEEE*, Shouhua Zhao, Zhixue Chen, Guoqiang Zhang, *Member, IEEE*, and Dianguo Xu, *Fellow, IEEE*

***Abstract*—In the voltage source inverter applications, inverter nonlinearities would affect the parameter identification process in many ways. Hence, this article proposes an offline identification method for resistance and *dq*-axis inductance surface by considering the inverter nonlinearity characteristics. A variable amplitude square-wave injection (VASI) scheme is proposed for the *dq*-axis inductance identification. The VASI method achieves the inductance identification with a novel data sampling strategy. Meanwhile, it can also establish the inductance surfaces by only a few identified data points with a polynomial fitting algorithm, which greatly reduces the identification time compared with the existing methods. The resistance identification is realized by a slope signal injection method, in which the effect of IGBT voltage drop is analyzed. In order to improve the identification accuracy, the inverter nonlinearities are compensated by a self-learning method considering the zero-axis voltage at different rotor positions. At the same time, the sampling error in zero current zones of abc-phases is researched. In order to verify the effectiveness and generality, the proposed method is carried out on two different test machines and confirmed by finite element analysis.**

***Index Terms*—Inverter nonlinearity self-learning, offline parameter identification, permanent magnet synchronous motor (PMSM), sampling error in zero current zones (ZCZS), zero-axis voltage.**

I. Introduction

PERMANENT magnet synchronous machines (PMSMs) have been commonly investigated and applied in the industry because of the flexible controllability and high torque density [1]−[6]. In recent decades, many PMSM control schemes have been proposed to meet the requirements of various application conditions. Meanwhile, almost all kinds of control schemes strongly rely on the machine parameters [7], [8]. Among all the parameter identification methods, the offline methods are more applicable and flexible for not wasting the online control resources [9], [10]. In order to better serve the motor control and realize the auto-tuning process in various control methods, the *dq*-axis inductances and the resistance should be identified.

The offline inductance identification generally relies on the signal injection, where the high frequency (HF) injection methods based on hysteresis control are most commonly used [10], [11]. The amplitudes of the injected *dq*-axis currents are adjusted in real time by hysteresis control to consider the cross-coupling effect [12]. The inductances are calculated by the differential operation of the *dq*-axis flux linkages estimated and stored in advance [12], [13], which are time-consuming and resource-consuming. The rotating signal injection method is another commonly applied offline inductance estimation strategy [14], [15]. Typically, a rotating double-direction pulse injection method was studied in [14], which identified inductance without the knowledge of the rotor position. However, the rotating signal-based method can hardly take into account the cross-coupling effect. The inductance identification methods by sinusoidal signal injection have been proposed in recent years. In [16], a sinusoidal voltage injection method was studied to estimate the spatial inductance map by scanning the rotor angle. By researching the PMSM impedance model, a small amplitude sinusoidal signal injection method was proposed in [17], and the inductance could be calculated from the phase information of injected signals. In [18], the *dq*-axis inductances considering the cross-coupling effect were obtained by injecting the composite signals of dc and HF sinusoidal signals, but the additional shaft locking device was needed. To sum up, it is still essential to study an offline inductance identification method considering cross-coupling with strong generality and simple operation.

The resistance plays an important role in the control strategy, self-commissioning process, and fault diagnosis of PMSMs [19], [20]. The most commonly used resistance identification methods are realized by two-level dc currents injection at standstill [21], [22]. This method is simple and practicable. However, it is easily affected by inverter nonlinearities and signal perturbations. In

Manuscript received March 4, 2021; revised May 11, 2021; accepted June 8, 2021. Date of publication June 16, 2021; date of current version August 16, 2021. This work was supported in part by the Research Fund for the National Natural Science Foundation of China (51961130385, 52007039, 51807037) and in part by Heilongjiang Provincial Postdoctoral Science Foundation under Grant LBH-TZ2013. Recommended for publication by Associate Editor A. Muetze. *(Corresponding author: Nannan Zhao.)*

Qiwei Wang, Nannan Zhao, Gaolin Wang, Guoqiang Zhang, and Dianguo Xu are with the School of Electrical Engineering and Automation, Harbin Institute of Technology, Harbin 150001, China (e-mail: wqw0543@163.com; znn429@126.com; wgl818@hit.edu.cn; zhgq@hit.edu.cn; xudiang@hit.edu.cn).

Shouhua Zhao and Zhixue Chen are with the China Railway Rolling Stock Corporation (CRRC), Zhuzhou Motor Co., Ltd., Zhuzhou 412000, China (e-mail: zxz_9999@163.com; 717895810@qq.com).

Color versions of one or more figures in this article are available at https://doi.org/10.1109/TPEL.2021.3089544.

Digital Object Identifier 10.1109/TPEL.2021.3089544

order to deal with the dead time effect, a short pulse voltage signal injection method was introduced in [23], where the resistance could be identified during the energy releasing process of the MOSFET. In [24] and [25], the resistance was estimated with the linear regression method by the *d*-axis slope current injection, which avoided the parasitic capacitance and reduced the sampling disturbance. Although the inverter nonlinearities have been widely studied in the resistance identification [9], the influence of insulated gate bipolar transistor (IGBT) voltage drop on resistance identification has not been analyzed yet [26]. Therefore, it is very important to investigate a resistance identification method considering all kinds of inverter nonlinearities with strong robustness.

Since the back electromotive force of PMSM remains zero in the offline parameter identification process, the inverter nonlinearities have a great influence on the parameter identification, which need to be compensated [27]. The parameter identification error caused by the dead time effect was analyzed and compensated with the sign function in [28] and [29]. For improving the compensation accuracy of the inverter nonlinearities at small current, a multiple linear regression fitting method was proposed based on the inverter physical model considering the parasitic capacitance [30]. In order to further improve the compensation effect of the inverter nonlinearity, a self-learning based method was studied by *d*-axis current injection in [24] and [32]. The abc-phase inverter nonlinearities were achieved with the characterization algorithm by dc current test in [27], where the rotor should be set at certain angles. However, in all the conventional methods, the impact of zero-axis voltage on the inverter nonlinearity compensation has not been considered yet. In conclusion, the inverter nonlinearity compensation method in the offline parameter identification still needs to be researched.

For further reducing the resource consumption and the identification time, an offline parameter identification method is investigated in this article. The main contributions are as follows. First, the resistance is estimated by the *d*-axis slope current injection. The effect of IGBT voltage drop is also compensated, which has not been analyzed yet in the resistance identification. Second, the inductance is identified with the variable amplitude square-wave injection (VASI) method, which simplifies the mathematical operation with a novel sampling strategy. Then, the *dq*-axis inductance surfaces are formed by a polynomial fitting based strategy with only a few identification data points further simplifying the identification process. Meanwhile, the *dq*-axis inverter nonlinearities can be learned simultaneously with the resistance identification, where the nonlinear effect of zero-axis voltage is considered for the first time. Finally, the sampling error in zero current zones (ZCZs) of abc-phases on the inductance identification is analyzed. The proposed algorithm is verified in two test machines.

This article is organized as follows. In Section II, the identification methods of the resistance and the inductance are presented. The inverter nonlinearity self-learning strategy is introduced in Section III, along with the compensation method of the sampling error in ZCZ. Experimental results and the finite element analysis (FEA) validation of the proposed algorithm are in Section VI.

II. Proposed Offline Parameter Identification Method

A. PMSM Model for Parameter Identification

The offline parameter identification is generally realized by the signal injection. Thus, the voltage equations, containing all the required parameters, can be adopted as the physical basis of parameter identification. The *dq*-axis voltage equations can be expressed with the flux linkage by

$$\begin{bmatrix} u_d \\ u_q \end{bmatrix} = R_s \begin{bmatrix} i_d \\ i_q \end{bmatrix} + \frac{\mathrm{d}}{\mathrm{d}t} \begin{bmatrix} \psi_d \\ \psi_q \end{bmatrix} + \omega_e \begin{bmatrix} -\psi_q \\ \psi_d \end{bmatrix} \tag{1}$$

where $u_{d,q}$ are the *dq*-axis voltages, $i_{d,q}$ are the *dq*-axis currents, R_s is the stator resistance, and ω_e is the rotation speed, which is 0 in offline condition. $\psi_{d,q}$ are the *dq*-axis flux linkages, satisfying $\psi_d = L_{d\_\mathrm{app}} i_d + \psi_m$ and $\psi_q = L_{q\_\mathrm{app}} i_q$, where ψ_m is the permanent magnet flux linkage.

The voltage equations with the inductance can be presented as follows:

$$\begin{aligned} \begin{bmatrix} u_d \\ u_q \end{bmatrix} = R_s \begin{bmatrix} i_d \\ i_q \end{bmatrix} + \begin{bmatrix} L_{d\_\mathrm{inc}} & 0 \\ 0 & L_{q\_\mathrm{inc}} \end{bmatrix} \frac{\mathrm{d}}{\mathrm{d}t} \begin{bmatrix} i_d \\ i_q \end{bmatrix} \\ + \omega_e \begin{bmatrix} 0 & -L_{q\_\mathrm{app}} \\ L_{d\_\mathrm{app}} & 0 \end{bmatrix} \begin{bmatrix} i_d \\ i_q \end{bmatrix} + \omega_e \begin{bmatrix} 0 \\ \psi_m \end{bmatrix} \end{aligned} \tag{2}$$

where L_{d,q_app} and L_{d,q_inc} are the *dq*-axis apparent inductances and the incremental inductances, respectively, which can be calculated by

$$\begin{cases} L_{x\_\mathrm{inc}} = \mathrm{d}\psi_x / \mathrm{d}i_x \\ L_{x\_\mathrm{app}} = \psi_x / i_x \end{cases} x = d, q. \tag{3}$$

Considering the magnetic saturation and the cross-coupling effect, L_{d,q_app} and L_{d,q_inc} are not the same. However, it is concluded in (3) that L_{d,q_app} and L_{d,q_inc} are mathematically equivalent, which is shown as

$$L_{x\_\mathrm{inc}} = \frac{\mathrm{d}(L_{x\_\mathrm{app}} i_x)}{\mathrm{d}i} x = d, q. \tag{4}$$

Hence, estimating only one kind of inductance is enough to obtain both. In this article, only L_{d,q_inc} is identified.

The whole parameter identification scheme is illustrated in Fig. 1, where i_{d_fdb} and i_{q_fdb} are the current feedbacks, and $i_d{}^*$ and $i_q{}^*$ are the *dq*-axis current references. The resistance R_s is first identified, and the inverter nonlinearity self-learning process can be executed in parallel. Then, the *dq*-axis inductance identification is carried out, along with the inductance surface forming process.

B. dq-Axis Inductance Identification and Sampling Strategy of VASI Method

The VASI method is introduced for inductance identification, where the square-wave voltage is injected for identifying the discrete inductance data, as presented in

$$u_x = \begin{cases} U_x, t \in (kT_x, (0.5+k)T_x) & k = 0, 1, 2 \ldots \\ -U_x, \mathrm{otherwise} & x = d, q. \end{cases} \tag{5}$$

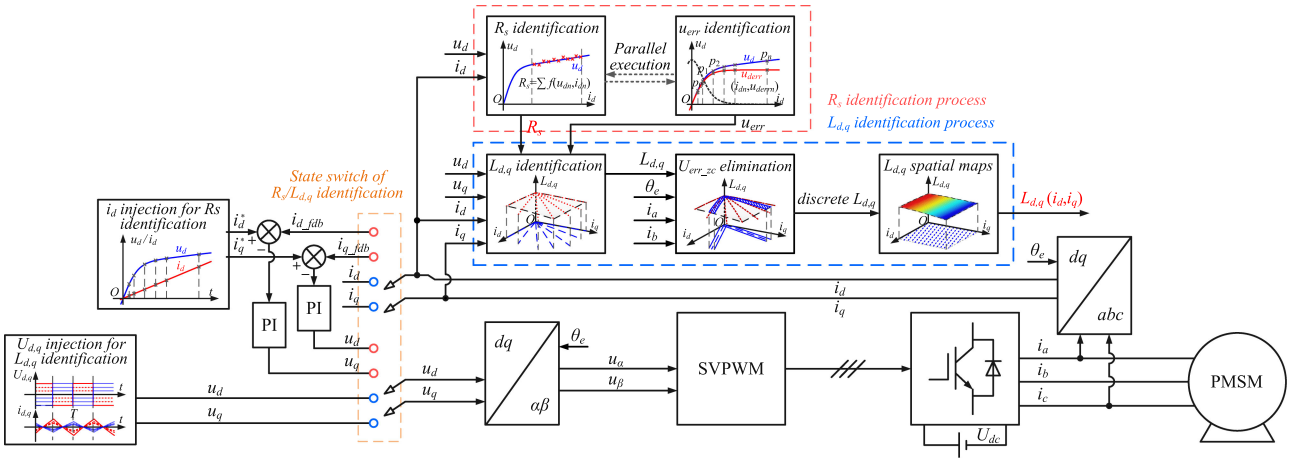

Fig. 1. Block diagram of the proposed parameter identification method.

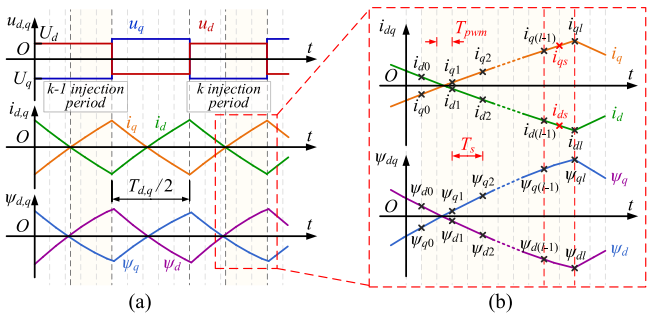

Fig. 2. Signal injection and data sampling scheme of the VASI method in the inductance identification process. (a) Voltage injection waveforms. (b) Data sampling in a single injection period.

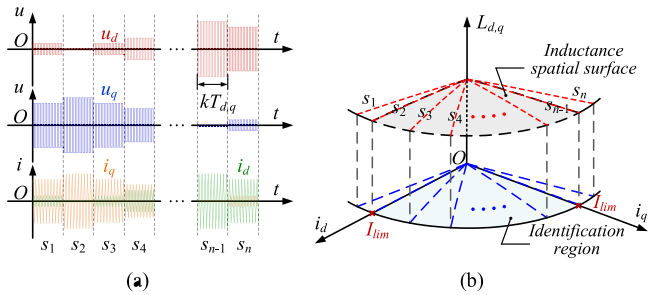

Fig. 3. Sampling trajectories and surface forming of the VASI method in the inductance identification process. (a) Signal injection scheme. (b) Sampling trajectories in the inductance surface.

where $U_{d,q}$ are the dq-axis voltage amplitudes, $T_{d,q}$ are the periods of the injected dq-axis voltages, and k is the count variable of $T_{d,q}$. In the inductance identification, the dq-axis flux is calculated at first, which is presented as

$$\psi_{xl} = \psi_{x(l-1)} + (u_{xl} - R_s i_{xl})T_s \; x = d, q \tag{6}$$

where T_s is the sampling period, which is $1-4$ times of the pulsewidth modulation (PWM) period $T_{\rm pwm}$, and l is the sampling number in one injection period. For identifying $L_{d,q}$, the values of $u_{d,q}$, $i_{d,q}$, and $\psi_{d,q}$ are sampled every sampling period, as shown in Fig. 2. For sampling enough data, $T_{d,q}$ are set as 20 times of T_s. In order to simulate the actual operation condition, the data are sampled in $i_d \le 0$ and $i_q \ge 0$.

$L_{d,q}$ can be directly calculated by the variation of $\psi_{d,q}$ and $i_{d,q}$ between two sampling points. For eliminating the disturbance errors, the average value of k_0 cycles is taken as the identified inductance. The corresponding currents $i_{d,qs}$ of the identified inductance are the average current of the two sampling points in k_0 cycles. The mathematical expressions are shown as

$$\begin{cases} L_x(\bar{i}_{ds}, \bar{i}_{qs}) = \frac{1}{k_0} \sum\limits_{k=1}^{k_0} \frac{\psi_{xl} - \psi_{x(l-1)}}{i_{xl} - i_{x(l-1)}} \\ \bar{i}_{xs} = \frac{1}{2k_0} \sum\limits_{k=1}^{k_0} i_{xl} + i_{x(l-1)} \end{cases} x = d, q. \tag{7}$$

In sum, a series of $L_{d,q}\,(i_{dn}, i_{qn})$ are estimated simultaneously with the signal injection process. The identification process is simplified compared with the conventional methods, where the identified $\psi_{d,q}$ needs to be first stored and processed after then [24].

C. VASI-Based Inductance Surface Forming Algorithm With Polynomial Fitting

In order to obtain the continuous inductance surface, the conventional hysteresis control based methods increase the identification points by increasing the injected $i_{d,q}$ combinations [13], [24]. However, it would prolong the identification time and rise the winding temperature, which will lead to the identification error. For solving the problem, a polynomial fitting-based inductance surface forming method is studied by the VASI method, which can generate the inductance surface by only a few identification data points.

By changing $u_{d,q}$ amplitudes, the VASI method can guarantee that $i_{d,q}$ covers the dq-axis current plane radially, corresponding to trajectories s_1-s_n in Fig. 3. s_1 and s_9, beyond the range of $L_{d,q}$ surfaces, are applied to form the $L_{d,q}$ in $i_d = 0$ and $i_q = 0$. With certain $u_{d,q}$, $L_{d,q}$ along each trajectory can be identified and sampled, as shown in (7) and Fig. 2. On the basis of all the sampling data of s_1-s_n, the polynomial fitting method is

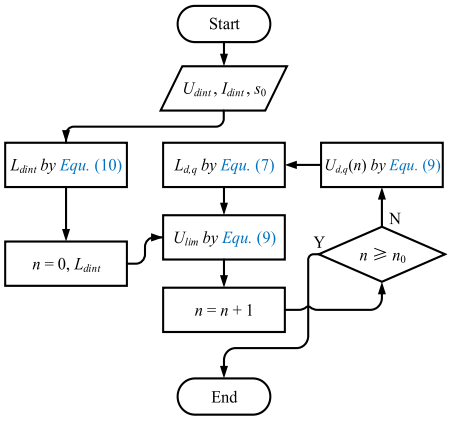

Fig. 4. Flowchart of the VASI method along with the $U_{\lim}$ selection.

proposed to form $L_{d,q}$ surfaces, as shown in Fig. 3(b). The fitting formula is as follows:

$$L_{d,q}(i_d, i_q) = a_{00} + a_{10}i_d + a_{01}i_q + \cdots + a_{pq}{i_d}^{p0}{i_q}^{q0} \quad (8)$$

where $a_{00}-a_{pq}$ are the surface fitting parameters, p_0 and q_0 are the orders of the fitting formula, the derivation of which is given in Appendix A.

The amplitudes of $u_{d,q}$ in the VASI method are selected by

$$\begin{cases} U_d(n)/U_q(n) = \tan(\pi n/2n_0) \\ U_q(n) = (U_{\lim}^2 - U_d(n)^2)^{0.5} \\ U_{\lim} = I_{\lim}R_s(1 + e^{-T_{dq}R_s/L_d})/ \\ \qquad (1 - e^{-T_{dq}R_s/L_d}) \end{cases} n = 1, 2, \ldots, n_0 \quad (9)$$

where $U_{\lim}$ and $I_{\lim}$ represent the limit values of the injected voltages and currents, respectively. $I_{\lim}$ is generally selected as $1-1.5$ p.u. n_0 is the number of all voltage combinations, corresponding to s_1-s_n in Fig. 3. n_0 can be selected as $8-15$, which can limit the identification time within 20 s

$$L_{dint} = \frac{T_d R_s}{ln(U_{dint} + I_{dint}R_s) - ln(U_{dint} - I_{dint}R_s)}. \quad (10)$$

In order to ensure that $i_{d,q}$ does not exceed $I_{\lim}$, the voltage $U_{\lim}$ should be determined in advance, which is carried out as follows: 1) a small-amplitude square wave voltage U_{dint} is injected into the d-axis; 2) after setting a current limitation I_{dint}, an initial value of d-axis inductance L_{dint} can be estimated by (10); 3) $U_{\lim}$ can be approximately obtained with L_{dint} by (9).

By (7)−(10), the VASI method is realized, along with the $U_{\lim}$ determination process, as illustrated in Fig. 4. In this case, the $L_{d,q}$ surface can be easily obtained with a few identification data points. And the fitting equation (8) can be directly applied in the machine control. However, in the conventional methods, $L_{d,q}$ surface is formed with the lookup table by sampling as much data points as possible, which increases the time and the complexity of the identification process.

D. Resistance Identification Strategy Considering IGBT Voltage Drop

Resistance is also important in the control, auto-tuning, and fault diagnosis of general-purpose PMSM drives, especially in low-speed operation [19], [20]. In addition, according to (6), R_s is needed for inductance identification. In this part, an estimation scheme is studied with the d-axis slope current injection, where the resistance can be calculated by linear regression with the values of the current reference and the induced voltage. Also, the effect of IGBT voltage drop is analyzed.

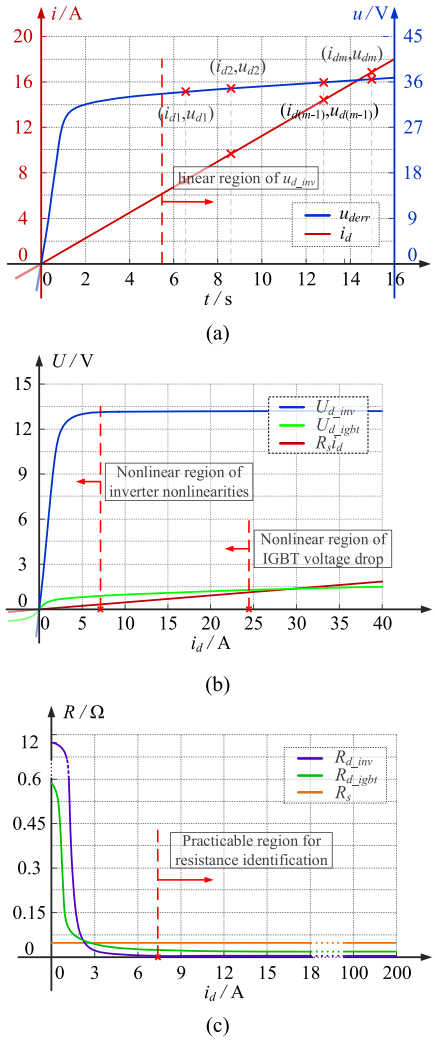

Fig. 5. Inverter nonlinearity characteristics in the R_s identification process. (a) u_d and i_d in the R_s identification process. (b) Voltage components in the R_s identification process. (c) Equivalent resistance in the R_s identification process.

In R_s identification process, the actual d-axis voltage u_d is affected by inverter nonlinearities, which is expressed by

$$\begin{cases} u_d = R_s i_d + u_{\text{derr}} = R_s i_d + u_{d\_\text{igbt}} + u_{d\_\text{inv}} \\ du_d/di_d = R_s + R_{d\_\text{igbt}} + R_{d\_\text{inv}} \end{cases} \quad (11)$$

where u_{derr} is the inverter nonlinearity voltage error. It contains the IGBT voltage drop u_{d_igbt} and other nonlinear voltage parts u_{d_inv}, including the dead time effect, parasitic capacitance effect, etc. [27]. Since the slope of the injected current and the variation of L_d are small, the current differential part is far less than the resistance itself, which is neglected in (11).

When the slope current is injected in d-axis, u_d behaves nonlinearly at small current range, as shown in Fig. 5(a). In

Fig. 5(b), the components of d-axis voltage are presented, which would affect the resistance identification result without the inverter nonlinearity compensation [24]. R_{d_inv} and R_{d_igbt} are the equivalent resistances of u_{d_igbt} and u_{d_inv} as shown in Fig. 5(c). R_{d_inv} is zero at large current, and R_{d_igbt} is generally nonlinear within the rated current of PMSM [31]. In the existing literatures, R_{d_igbt} is ignored for its relatively small value. However, in the resistance identification, R_{d_igbt} should be considered, especially for the PMSM with small resistance.

Since IGBTs in the abc-phases are the same, the IGBT voltage drop at dq-axes can be compensated through the coordinate transformation with a single-phase IGBT voltage drop, as given in

$$u_{d\_\mathrm{igbt}} = \tfrac{2}{3}(u_{a\_\mathrm{igbt}}\cos\theta_e + u_{b\_\mathrm{igbt}}\cos(\theta_e - \tfrac{2}{3}\pi) + u_{c\_\mathrm{igbt}}\cos(\theta_e + \tfrac{2}{3}\pi)) \tag{12}$$

where θ_e is the initial rotor position. θ_e can be estimated offline by the sensorless drives scheme in [3]. IGBT voltage drop in each phase u_{abc_igbt} can be obtained from the datasheet. In order to avoid the influence of u_{d_inv}, the injected current should guarantee that the induced voltage exceeds the nonlinear region and R_s is identified in the inverter linear region as shown in Fig. 5. By substituting (12) into (11), R_s can be obtained by linear regression in (13) with m sampling points to eliminate the undesired disturbance error

$$R_s = \frac{m\sum i_d(u_d - u_{d\_\mathrm{igbt}}(i_d)) - \sum(u_d - u_{d\_\mathrm{igbt}}(i_d))\sum i_d}{m\sum {i_d}^2 - (\sum i_d)^2}. \tag{13}$$

III. Error Analysis and Compensation Strategy of Offline Inductance Identification

A. Inverter Nonlinearities Compensation Considering Zero-Axis Voltage

For identifying $L_{d,q}$ accurately, it is necessary to obtain and compensate $u_{d\mathrm{err}}(i_d)$ and $u_{q\mathrm{err}}(i_q)$ during the dq-axis inductance identification process [27], [30]. Considering the inverter nonlinearities, (6) should be modified into

$$L_x = (u_x - u_{x\mathrm{err}}(i_x) - R_s i_x)T_s/\mathrm{d}i_x \quad x = d, q. \tag{14}$$

In (11), $u_{d\mathrm{err}}$ (i_d) can be obtained simultaneously in the R_s identification process. As for $u_{q\mathrm{err}}$ (i_q), in the conventional methods, $u_{d\mathrm{err}}$ (i_d) is applied to calculate the abc-phase voltage error $u_{abc\mathrm{err}}$ (i_{abc}). Then, $u_{q\mathrm{err}}$ (i_q) can be calculated with $u_{abc\mathrm{err}}$ (i_{abc}) [24]. The whole process is explained as follows:

$$\begin{cases} \begin{bmatrix} x_d \\ x_0 \end{bmatrix} = \frac{2}{3}\begin{bmatrix} C_{d\to abc} \\ C_{0\to abc} \end{bmatrix} x_{abc} \quad x = u_{\mathrm{err}}, i\ . \\ x_{abc} = C_{abc\to dq0}x_{d,q} \end{cases} \tag{15}$$

Generally, $u_{0\mathrm{err}}$ and i_0 are considered to be zero in coordinate transformations [32]. According to Kirchhoff's current law in the Y-connected winding, i_0 is always zero. However, $u_{0\mathrm{err}}$ is not always zero with inverter nonlinearities, which is expressed by

$$\begin{cases} i_0 = i_a + i_b + i_c \equiv 0 \\ u_{0\mathrm{err}} = u_{a\mathrm{err}}(i_a) + u_{b\mathrm{err}}(i_a) + u_{c\mathrm{err}}(i_a) \not\equiv 0 \end{cases} \tag{16}$$

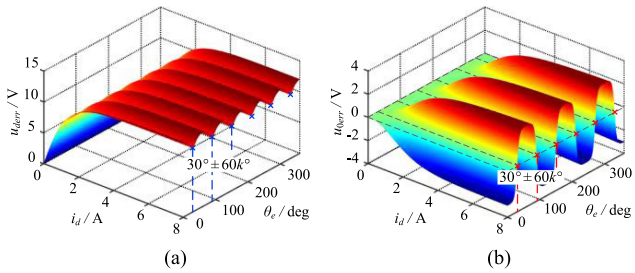

Fig. 6. Variation of $u_{d\mathrm{err}}$ and $u_{0\mathrm{err}}$ versus the rotor position θ_e and injected i_d in R_s identification process. (a) Variation of $u_{d\mathrm{err}}$. (b) Variation of $u_{0\mathrm{err}}$.

The nonzero $u_{0\mathrm{err}}$ in the inverter nonlinearity compensation should be considered, which has not been studied yet. With the simulation model in [25], the variations of $u_{d\mathrm{err}}$ and $u_{0\mathrm{err}}$ versus θ_e and i_d are shown in Fig. 6. $u_{d\mathrm{err}}$ changes periodically with θ_e and shows a saturable increase with i_d. As for $u_{0\mathrm{err}}$, there is a third pulsation in one electrical cycle, in which $u_{0\mathrm{err}}$ is zero only at $\theta_e = 30° \pm 60k°$.

Since $u_{0\mathrm{err}}$ is not always zero, the conventional inverter nonlinearity compensation methods are no longer accurate. In this case, for still obtaining $u_{d,q\mathrm{err}}$ $(i_{d,q})$ in (15), an inverter nonlinearity compensation method considering $u_{0\mathrm{err}}$ is studied under different θ_e, which is realized simultaneously with the R_s identification process. Taking a-phase inverter nonlinearity voltage $u_{a\mathrm{err}}$ (i_a) as an example, when the R_s identification process is carried out, $u_{a\mathrm{err}}$ (i_a) is calculated as follows.

1) When $\theta_e = 30° \pm 60k°$, $u_{a\mathrm{err}}$ (i_a) can be calculated by

$$u_{a\mathrm{err}}(i_a) = u_{d\mathrm{err}}(i_a/\cos(\theta_e))\cos(\theta_e). \tag{17}$$

2) When $\theta_e = 0° \pm 60k°$, $u_{a\mathrm{err}}$ (i_a) can be calculated by

$$u_{a\mathrm{err}}(i_a) = \frac{2}{3}\left[\sum_0^h u_{d\mathrm{err}}(2^{-2h}i_d) - \sum_0^h u_{d\mathrm{err}}\left(2^{-2h+1}i_d\right)\right]. \tag{18}$$

3) When θ_e is an arbitrary value, the general expression of $u_{a\mathrm{err}}$ (i_a) is derived by the piecewise linear interpolation (PLI) as

$$u_{a\mathrm{err}}(i_a) \approx \frac{i_j - i_a}{i_j - i_{j-1}}U_{j-1} + \frac{i_a - i_{j-1}}{i_j - i_{j-1}}U_j = M(i_a)U_{j-1} + N(i_a)U_j \tag{19}$$

where M and N represent the weights of the sampling voltage U_j.

The abc-phase inverter nonlinearity voltages considering $u_{0\mathrm{err}}$ can be accurately calculated by (17)−(19) at any θ_e, the detailed derivation of which is given in Appendix B. In practice, (17)−(19) should be applied by the following rules.

1) When the rotor rotation is allowed, the rotor can be positioned at $30° \pm 60k°$ or $0° \pm 60k°$. In this case, (17) and (18) are applied, which are efficient and simple in the calculation process.

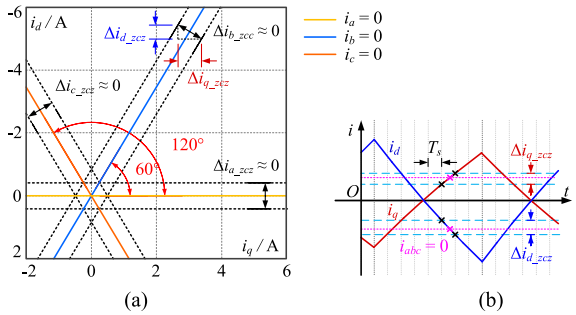

Fig. 7. Distributions of ZCZs in abc-phases and dq axes. (a) abc-Phase ZCZs in $i_{d,q}$ plane. (b) Relationship between the width of abc-phase ZCZs and the induced i_{dq}.

2) When the rotor rotation is forbidden, (19) is used for arbitrary rotor position.
3) After calculating u_{abcerr} (i_{abc}), the values of u_{derr} (i_d) and u_{qerr} (i_q) are then obtained by (15). And inverter nonlinearities can be finally compensated with (14).

B. Correction Strategy of Sampling Error in Zero Current Zones of abc-Phase

The parasitic capacitance effect results in a large equivalent resistance in ZCZs of abc-phases. Therefore, the induced $i_{d,q}$ are greatly reduced, which amplifies the influence of the sampling error and eventually affects $L_{d,q}$ identification [25]. As the inherent property of voltage source inverter, the sampling error cannot be compensated. Hence, the correction method for the sampling error in abc-phase ZCZs needs to be studied

$$\begin{cases} i_a = i_d\cos(\omega_e t+\theta_e) - i_q\sin(\omega_e t+\theta_e) = 0 \\ i_b = i_d\cos(\omega_e t+\theta_e-\frac{2\pi}{3}) - i_q\sin(\omega_e t+\theta_e-\frac{2\pi}{3}) = 0 \\ i_c = i_d\cos(\omega_e t+\theta_e+\frac{2\pi}{3}) - i_q\sin(\omega_e t+\theta_e+\frac{2\pi}{3}) = 0. \end{cases} \tag{20}$$

With the *dq*-axis signal injection, the zero currents of abc-phases in $i_{d,q}$ plane can be expressed as (20). At $\theta e = 0°$, the distribution of the zero currents in $i_{d,q}$ plane are illustrated in Fig. 7, where the angles between zero current lines are 60°. The dotted lines in Fig. 7(a) present the width of the abc-phase ZCZs Δi_{abc_zcz}.

Fig. 7(b) shows the relationship between Δi_{abc_zcz} and the width of the induced *dq*-axis current $\Delta i_{d,q\_zcz}$. It can be seen that the ZCZ sampling error only affects the $L_{d,q}$ in the *dq*-axis sampling periods containing the abc-phase zero currents. The mathematical expression of the relationship between Δi_{abc_zcz} and $\Delta i_{d,q\_zcz}$ is given by

$$\Delta i_{abc\_zcc} = \sqrt{\Delta {i_{d\_zcc}}^2 + \Delta {i_{q\_zcc}}^2}. \tag{21}$$

In order to deal with the $L_{d,q}$ identification results influenced by the ZCZ sampling error, all the sampled $L_{d,q}$ should be checked whether the sampled periods contain the abc-phase zero currents expressed by (20) and (21). If so, the error data could be directly eliminated, and $L_{d,q}$ surfaces could be formed with the rest of the data with (8). Since the ZCZ sampling error affects only one sampling period, the error data is of low proportion in the whole inductance data, which hardly affects the polynomial fitting process.

TABLE I
PARAMETERS OF TEST MACHINES

Parameters	1.6kW SPMSM	25kW IPMSM
Rated voltage (V)	200	380
Rated current (A)	5	70
Stator resistance (Ω)	1.38	0.0456
No load *d*-axis inductance (mH)	4.242	0.354
No load *q*-axis inductance (mH)	4.650	0.825

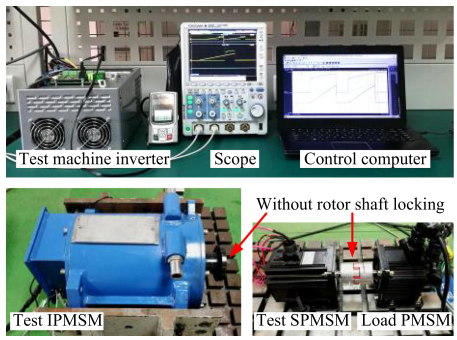

Fig. 8. Test platforms of 25-kW IPMSM and 1.6-kW SPMSM.

TABLE II
AMPLITUDES OF THE *DQ*-AXIS INJECTED VOLTAGE AND THE *DQ*-AXIS INDUCED CURRENT

Items	s_1	s_2	s_3	s_4	s_5	s_6	s_7	s_8	s_9
U_d/V	10.4	0	10.4	20.0	28.3	34.6	38.6	40.0	38.6
U_q/V	38.6	40.0	38.6	34.6	28.3	20.0	10.4	0	10.4
I_d/A	2.29	0.19	2.51	3.69	4.76	6.18	7.08	8.51	7.12
I_q/A	7.31	8.01	7.85	7.51	6.48	4.27	1.79	0.14	1.51

IV. EXPERIMENTAL RESULTS

The proposed method is carried out on a 22-kW drive. The ARM STM32F103 and IGBT IKP40N65H5 are adopted. The PWM switching frequency is 6 kHz, and the dead time is 3.2 μs. In order to verify the generality of the proposed algorithm, two PMSMs with different structures surface permanent magnet synchronous machine (SPMSM) and interior permanent magnet synchronous machine (IPMSM) are tested, the parameters of which are very different. The rated parameters of two test PMSMs are given in Table I.

Fig. 8 shows the overall control platform, where the rotor shafts of the machines are not necessarily locked. The FEA results have been taken as a reference for the evaluation of the proposed method, where the frozen permeability method is adopted to calculate the incremental inductance.

Taking the 1.6-kW SPMSM as an example, the waveforms of the whole VASI inductance identification process are presented in Fig. 9. For s_1-s_9 in Fig. 9(a), $U_{d,q}$ are variables by (9) realizing the $L_{d,q}$ identification under different $i_{d,q}$ combinations, the values of which are presented in Table II. Fig. 9(b) and (c)

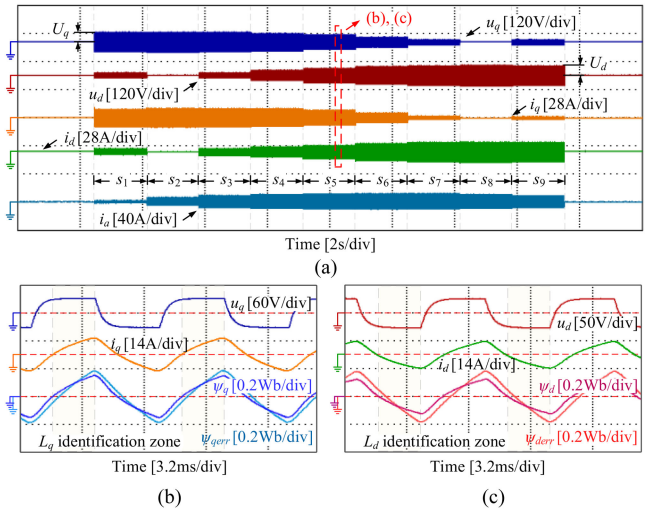

Fig. 9. Experimental waveforms of the VASI method during the whole $L_{d,q}$ identification process. (a) Overall waveforms of $u_{d,q}$ and $i_{d,q}$. (b) Detailed waveforms of u_d, i_d, and ψ_d. (c) Detailed waveforms of u_q, i_q, and ψ_q.

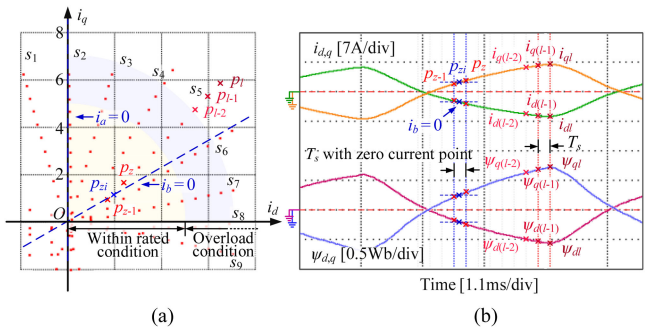

Fig. 10. Distribution of the sampling points of the VASI method in $i_{d,q}$ plane and the data sampling method. (a) Distribution of the sampling points in $i_{d,q}$ plane. (b) Sampling strategy for $L_{d,q}$ identification.

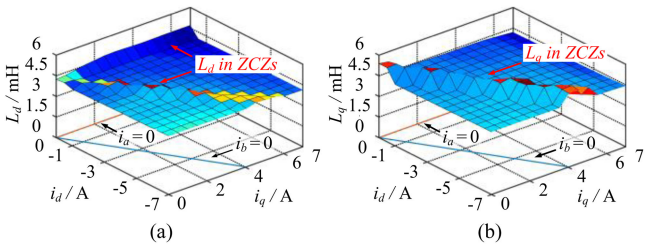

Fig. 11. Experimental results of identified $L_{d,q}$ including the sampling error in ZCCs at $\theta_e = 0°$. (a) L_d of 1.6-kW SPMSM. (b) L_q of 1.6-kW SPMSM.

presents the detailed waveforms of $u_{d,q}$, $i_{d,q}$, and $\psi_{d,q}$ under s_5 condition, which are only sampled at $i_d < 0$ and $i_q > 0$. The dq-axis injection frequencies are set as 150 Hz. $\psi_{d,q}$ and $\psi_{d,q\mathrm{err}}$, corresponding to the flux linkages before and after the inverter nonlinearity compensation, are obviously different. Hence, the inverter nonlinearity compensation is essential, whose effect is shown in Figs. 12 and 13. With the VASI method, the whole inductance identification process can be accomplished within 20 s.

Fig. 10 shows the distribution of the sampling points of the VASI method in $i_{d,q}$ plane. The sampling trajectories $s_1 - s_9$ correspond to the $u_{d,q}$ combinations in Fig. 9(a). Taking s_5 as an example, the number of sampling points l is 12 for each sampling trajectory, satisfying $T_s = 2T_{\mathrm{pwm}}$, as shown in Fig. 10(b). In each sampling point, $u_{d,q}$, $i_{d,q}$, and $\psi_{d,q}$ are extracted at points $p_{l\text{-}2}$ to p_l. $L_{d,q}$ can be then identified by (7). The blue dotted lines in Fig. 10(a) illustrate the abc-phase zero currents.

In Fig. 10(b), the b-phase zero current line is between the sampling points p_z and $p_{z\text{-}1}$, where p_{zi} is the intersection point of s_6 and $i_b = 0$. According to Section III-B, the sampling data of p_z and $p_{z\text{-}1}$ should be eliminated to deal with the sampling error in ZCCs.

Fig. 11 shows the identified $L_{d,q}$ of 1.6-kW SPMSM at $\theta_e = 0°$ with the sampling error data in ZCCs. It is obvious that $L_{d,q}$ near 0°, 60°, and 120° in $i_{d,q}$ plane are distorted, which proves the existence of the ZCC sampling error. It can be seen that although the inverter nonlinearity compensation has been carried out, the sampling error in ZCCs can still not be compensated. As presented in Fig. 10, the error data is only a small portion of the whole identified $L_{d,q}$ data in $i_{d,q}$ plane, which makes it reasonable to screen out the data in ZCCs and fit $L_{d,q}$ surfaces with the remaining data. It is worth noting that the L_q at $i_a = 0$ is not affected by the sampling error as shown in Fig. 11(b) because the a-phase voltage and current at 0°, including the sampling errors, are not involved at all in the dq-axis coordinate transformation.

Fig. 12 presents the influence of $u_{0\mathrm{err}}$ on the inverter nonlinearity compensation. For explaining this influence, the sampled inverter nonlinearity voltage $u_{d\mathrm{err\_spl}}$ is compared with the reconstructed voltage $u_{d\mathrm{err\_rec}}$ by (15) with d-axis slope current injection. Since the calculation process in (15) involves $u_{0\mathrm{err}}$, if $u_{0\mathrm{err}}$ is assumed to be 0 as in the conventional methods, $u_{d\mathrm{err\_spl}}$ and $u_{d\mathrm{err\_rec}}$ would be equal and vice versa. In this test, two groups of experiments are carried out where i_d is injected in 0° and 30°, respectively. It is shown in Fig. 12(a)−(e) that $u_{d\mathrm{err\_spl}}$ and $u_{d\mathrm{err\_rec}}$ are not the same at 0°. However, $u_{d\mathrm{err\_spl}}$ and $u_{d\mathrm{err\_rec}}$ coincide at 30° as shown in Fig. 12(f)−(J). $u_{0\mathrm{err}}$ is verified to be not always 0 in the coordinate transformation. It is also confirmed that $u_{0\mathrm{err}}$ is zero at 30° and is nonzero at 0°, which is consistent with the analysis in Fig. 6.

Fig. 13(a) shows the comparison of the inverter nonlinearity voltage $u_{d\mathrm{err\_spl}}$ sampled at 0° and the reconstructed voltage $u_{d\mathrm{err\_rec}}$ without inverter nonlinearity compensation. The error between $u_{d\mathrm{err\_spl}}$ and $u_{d\mathrm{err\_rec}}$ exists at any θ_e, which corresponds to Fig. 12(a)−(e). The variation trend of $u_{d\mathrm{err\_spl}}$ versus θ_e and i_d is consistent with that in Fig. 6(a). Fig. 13(b) illustrates $u_{d\mathrm{err\_spl}}$ and $u_{d\mathrm{err\_rec}}$ with the inverter nonlinearity compensation, as investigated in Section IV-A. $u_{d\mathrm{err\_spl}}$ is in good coincidence with $u_{d\mathrm{err\_rec}}$ in the test surface at any θ_e, which proves the effectiveness of the inverter nonlinearity compensation method considering $u_{0\mathrm{err}}$.

In Fig. 14, the resistance identification is realized at large i_d, and the experimental waveforms show the good convergence. The identified R_s of 1.6-kW SPMSM is between 1.365 and 1.473 Ω in Fig. 14(a), and the identification error is within 5% for the nameplate value. The identified R_s of 25-kW IPMSM

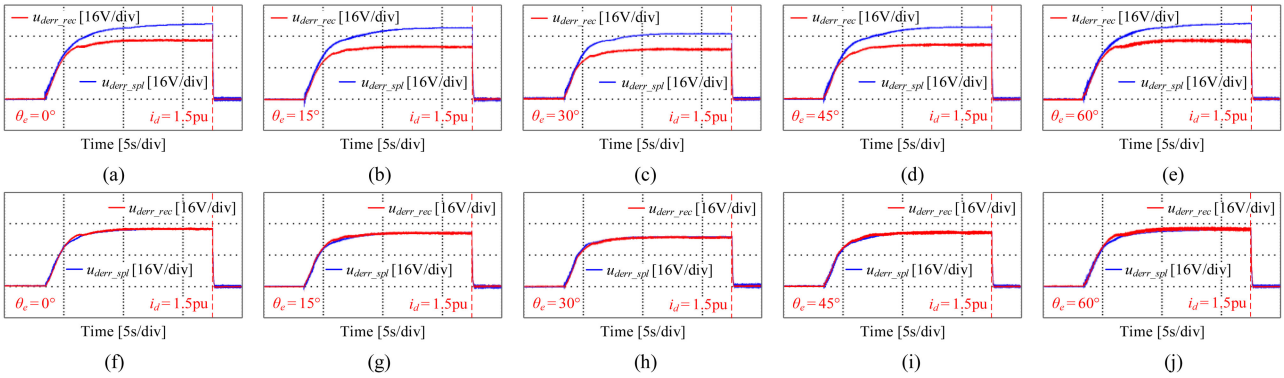

Fig. 12. Sampled inverter nonlinearity voltages and reconstructed voltages considering $u_{0\mathrm{err}}$ with d-axis slope current injection. (a) $u_{\mathrm{derr\_spl}}$ at 0° and reconstructed at 0°. (b) $u_{\mathrm{derr\_spl}}$ at 0° and $u_{\mathrm{derr\_rec}}$ at 15°. (c) $u_{\mathrm{derr\_spl}}$ at 0° and $u_{\mathrm{derr\_rec}}$ at 30°. (d) $u_{\mathrm{derr\_spl}}$ at 0° and $u_{\mathrm{derr\_rec}}$ at 45°. (e) $u_{\mathrm{derr\_spl}}$ at 0° and $u_{\mathrm{derr\_rec}}$ at 60°. (f) $u_{\mathrm{derr\_spl}}$ at 30° and $u_{\mathrm{derr\_rec}}$ at 0°. (g) $u_{\mathrm{derr\_spl}}$ at 30° and $u_{\mathrm{derr\_rec}}$ at 15°. (h) $u_{\mathrm{derr\_spl}}$ at 30° and $u_{\mathrm{derr\_rec}}$ at 30°. (i) $u_{\mathrm{derr\_spl}}$ at 30° and $u_{\mathrm{derr\_rec}}$ at 45°. (j) $u_{\mathrm{derr\_spl}}$ at 30°and $u_{\mathrm{derr\_rec}}$ at 60°.

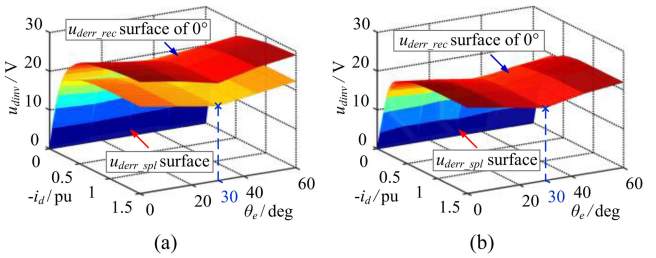

Fig. 13. Effect of the inverter nonlinearity compensation considering $u_{0\mathrm{err}}$. (a) $u_{\mathrm{derr\_spl}}$ at 0° and $u_{\mathrm{derr\_rec}}$ without compensation. (b) $u_{\mathrm{derr\_spl}}$ at 0° and $u_{\mathrm{derr\_rec}}$ with compensation.

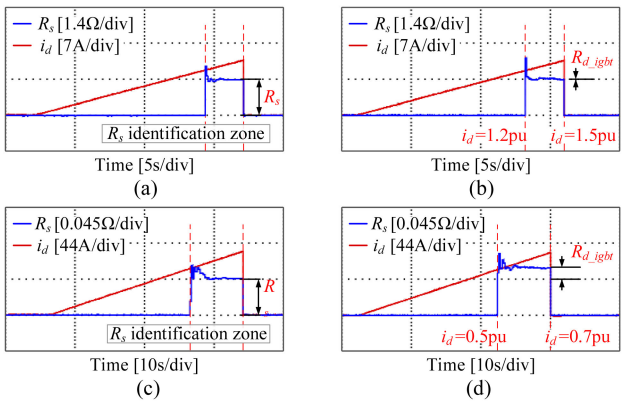

Fig. 14. Resistance identification results considering the IGBT voltage drop. (a) 1.6-kW SPMSM with u_{d_igbt} compensation. (b) 1.6-kW SPMSM without u_{d_igbt} compensation. (c) 25-kW IPMSM with u_{d_igbt} compensation. (d) 25-kW IPMSM without u_{d_igbt} compensation.

is between 0.0451 and 0.0467 Ω in Fig. 14(c), where the identification error is within 4%. When the IGBT voltage drop is not compensated, the error of the identified R_s exists as the R_{d_igbt} shown in Fig. 14(c) and (d). However, R_{d_igbt} of 25-kW IPMSM is far more obvious than that of 1.6-kW SPMSM. The reason is that R_s of 25-kW IPMSM is small enough to be affected by R_{d_igbt} which is about 0.015 Ω for the adopted IGBT.

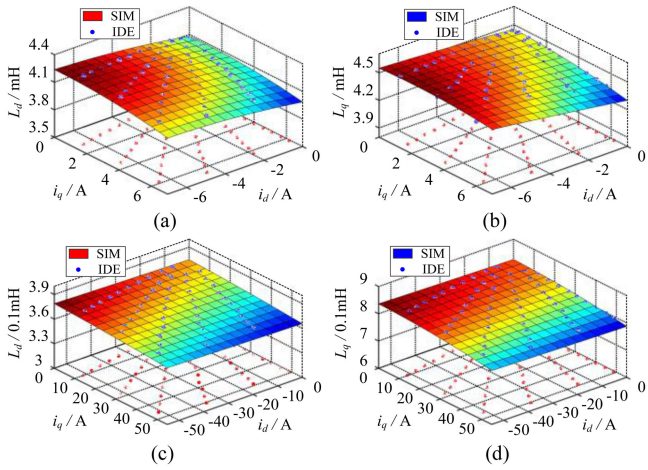

Fig. 15. Sampling trajectories and experimental results of $L_{d,q}$ without sampling error in ZCZs. (a) L_d of 1.6-kW SPMSM. (b) L_q of 1.6-kW SPMSM. (c) L_d of 25-kW IPMSM. (d) L_q of 25-kW IPMSM.

Therefore, the effectiveness of the R_s identification algorithm and the compensation method for the IGBT voltage drop are verified.

After the inverter nonlinearity compensation and the ZCZ sampling error correction, the identified $L_{d,q}$ (IDE) with the interpolation plane by simulation (SIM) are illustrated in Fig. 15. The sampling trajectories are also presented in dq-axis current plane. According to the identified results in Fig. 15, L_d and L_q increase with the decrease of i_d and vice versa since the magnetic saturation of the stator is affected by the demagnetization current. Similarly, with the increase of i_q, the magnetic saturation degree will be aggravated, which makes L_d and L_q decrease and vice versa. The unsaturated L_d and L_q values are 4.33 and 4.56 mH for 1.6-kW PMSM, and 0.376 and 0.832 mH for 25-kW PMSM, respectively, which are consistent with the nameplate values.

For $L_{d,q}$ surface fitting, two parameters p_0 and q_0 should be properly selected to determine (8). As explained in Appendix A, the polynomial determinant R^2 is introduced to evaluate the

TABLE III
DETERMINATION COEFFICIENT OF *DQ*-AXIS INDUCTANCE POLYNOMIAL SURFACE FITTING

R^2 of L_{dq}	$p_0=1$, $q_0=1$	$p_0=1$, $q_0=2$	$p_0=2$, $q_0=1$	**$p_0=2$, $q_0=2$**	$p_0=1$, $q_0=3$	$p_0=3$, $q_0=1$
1.6 L_d	0.93	0.96	0.96	**0.98**	0.96	0.96
1.6 L_q	0.89	0.96	0.90	**0.96**	0.97	0.91
25 L_d	0.97	0.98	0.97	**0.98**	0.98	0.98
25 L_q	0.96	0.99	0.96	**0.99**	0.99	0.96

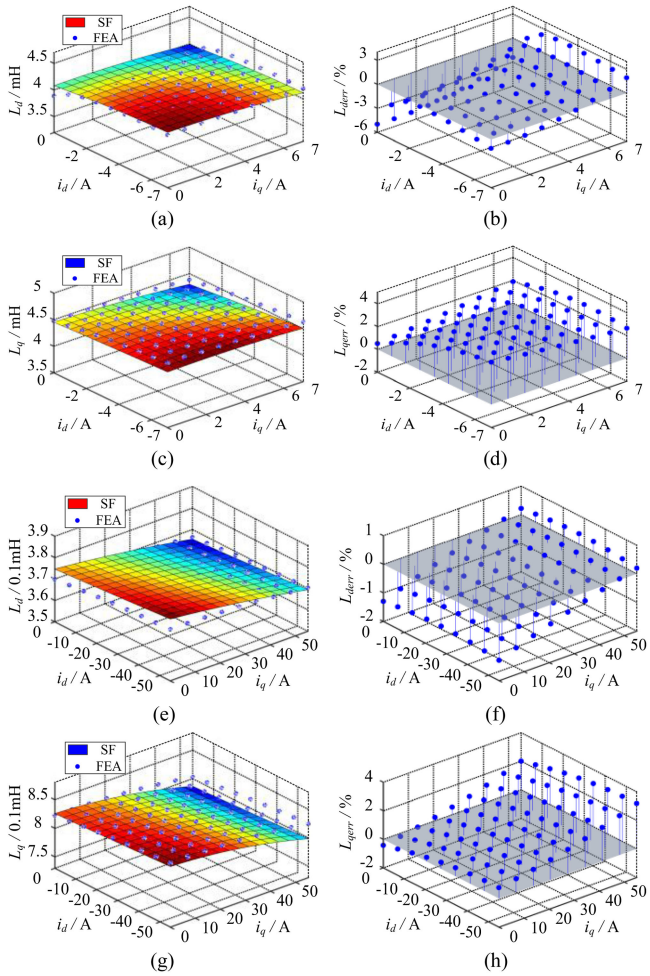

Fig. 16. Polynomial fitting and FEA results of $L_{d,q}$ without sampling error in ZCZs. (a) L_d of 1.6-kW SPMSM. (b) L_d error of 1.6-kW SPMSM. (c) L_q of 1.6-kW SPMSM. (d) L_q error of 1.6-kW SPMSM. (e) L_d of 25-kW IPMSM. (f) L_d error of 25-kW IPMSM. (g) L_q of 25-kW IPMSM. (h) L_q error of 25-kW IPMSM.

fitting effect of (8) under different p_0 and q_0 combinations. The closer R^2 is to 1, the better the fitting of $L_{d,q}$ surfaces will be. In addition, p_0 and q_0 should not be chosen too large considering the computation complexity. Table III gives the determination coefficient R^2 under different p_0 and q_0 combinations. It is concluded that $p_0 = 2$ and $q_0 = 2$ are suitable for accurately fitting the $L_{d,q}$ surface, as shown in Fig. 16.

Fig. 16(a), (c), (e), and (g) shows the comparison between the polynomial surface fitting results and the FEA results of $L_{d,q}$. Fig. 16(b), (d), (f), and (h) presents the error between the surface fitted results and the FEA results. The identification error of $L_{d,q}$ for 1.6-kW PMSM is less than 6%. Meanwhile, the identification error of $L_{d,q}$ for 25-kW PMSM is less than 4%. The effectiveness of the proposed polynomial fitting method is confirmed. Also, it is proved that the fitting polynomial (8) can be obtained by the limited data points in Fig. 15. Furthermore, the $L_{d,q}$ fitted in (8) can be directly applied in the machine control, which is much simpler than the conventional methods with the lookup table.

V. CONCLUSION

In this article, a novel offline parameter identification method was proposed. The resistance identification considers the inverter nonlinearities including the IGBT voltage drop, which improves the identification accuracy. As for the inductance identification, the VASI method can be carried out without the data storage of flux linkage and the differential mathematical calculations, which is simpler than the conventional hysteresis control-based methods. With the polynomial fitting algorithm, the inductance surface can be formed by only a few identified data points reducing the time and control resource consumption compared with the conventional methods. Furthermore, the inverter nonlinearity voltage can be estimated considering the zero-axis voltage simultaneously with the resistance identification process, which realizes the accurate inverter nonlinearity compensation at any rotor position. Meanwhile, the inductance identification error caused by the sampling error near ZCZs is also analyzed and compensated. The effectiveness and generality of the proposed method have been proved by the experimental and FEA results.

APPENDIX A

If the function $f(x, y)$ is continuous and integrable in the domain of definition. $f(x, y)$ can be fitted by the polynomial with limited number of sampling data $(x, y, f(x, y))$, which can be expressed by

$$\begin{cases} f(x,y) = a_{00} + a_{10}x + a_{01}y + a_{20}x^2 \\ \qquad\qquad + a_{02}y^2 + \cdots + a_{pq}x^p y^q \\ p = 1, 2, \ldots, p_0 \\ q = 1, 2, \ldots, q_0 \\ p + q \le p_0 \,\&\, p + q \le q_0 \end{cases} \tag{A1}$$

where $a_{00}-a_{pq}$ are the surface fitting parameters, which are derived by the recursive least squares (RLS) with the sampling data.

The $L_{d,q}$ surface can be equivalent to such a function. All the sampling data from the VASI method are applied for the polynomial fitting. The RLS equation is presented in (A2) to calculate $a_{00}-a_{pq}$.

$$\begin{cases} \boldsymbol{e} = \boldsymbol{y} - \boldsymbol{\lambda}^T \boldsymbol{\rho} \\ \boldsymbol{y}^T = [L_{d,q}(i_d, i_q)] \\ \boldsymbol{\lambda}^T = [1 i_d i_q \cdots {i_d}^{p0} {i_d}^{q0}] \\ \boldsymbol{\rho}^T = [a_{00} a_{10} a_{01} \cdots a_{pq}]. \end{cases} \tag{A2}$$

For verifying the fitting effect accuracy, the determination coefficient R^2 is introduced, as shown in (A3). The closer R^2 is to 1, the better the fitting effect will be

$$R^2 = 1 - \sum_{i=0}^{s} (f_i - \hat{f}_i)^2 \Big/ \sum_{i=0}^{s} (f_i - \bar{f})^2 \tag{A3}$$

where f_i is the ith sampling value, $\hat{f}_i$ is the ith fitted value, and $\bar{f}$ is the average of all y_i.

APPENDIX B

The inverter nonlinearity compensation methods considering $u_{0\mathrm{err}}$ are discussed at different θ_e. When the R_s identification process is carried out at different θ_e, the inverter nonlinearity of a-phase voltage is calculated as follows.

1) When $\theta_e = 30° \pm 60k°$, $u_{0\mathrm{err}} = 0$ and $i_0 = 0$. The relationship of u_d, i_d, u_a, and i_a can be expressed as

$$\begin{cases} i_a = i_d \cos\theta_e \\ u_a = u_d \cos\theta_e. \end{cases} \tag{A4}$$

By substituting (A4) into (15), $u_{a\mathrm{err}}$ (i_a) can be calculated by (17).

2) When $\theta_e = 0° \pm 60k°$, $u_{0\mathrm{err}} \neq 0$. The inverter nonlinearity characteristics of bc-phase are the same. In this case, (15) can be written as the following iterative form:

$$\begin{cases} 1.5u_{d\mathrm{err}}(i_d) = u_{a\mathrm{err}}(2^{-1}i_a) + u_{a\mathrm{err}}(i_a) \\ 1.5u_{d\mathrm{err}}(2^{-1}i_d) = u_{a\mathrm{err}}(2^{-2}i_a) + u_{a\mathrm{err}}(2^{-1}i_a) \\ 1.5u_{d\mathrm{err}}(2^{-2}i_d) = u_{a\mathrm{err}}(2^{-3}i_a) + u_{a\mathrm{err}}(2^{-2}i_a) \\ \vdots \\ 1.5u_{d\mathrm{err}}(2^{-2h+1}i_d) = u_{a\mathrm{err}}(2^{-2h}i_a) + u_{a\mathrm{err}}(2^{-2h+1}i_a). \end{cases} \tag{A5}$$

With the increase of the iteration number h, i_a tends to 0. According to Fig. 6(c), $u_{a\mathrm{err}}$ also tends to 0. Combined with (A5), the $u_{a\mathrm{err}}$ (i_a) can be obtained by

$$\begin{aligned} u_{a\mathrm{err}}(i_a) &= \frac{2}{3}\left[\sum_{0}^{h} u_{d\mathrm{err}}(2^{-2h}i_d) - \sum_{0}^{h} u_{d\mathrm{err}}(2^{-2h+1}i_d)\right] \\ &\quad + u_{d\mathrm{err}}(2^{-2h+1}i_d) \\ &\approx \frac{2}{3}\left[\sum_{0}^{h} u_{d\mathrm{err}}(2^{-2h}i_d) - \sum_{0}^{h} u_{d\mathrm{err}}(2^{-2h+1}i_d)\right]. \end{aligned} \tag{A6}$$

2) When θ_e is an arbitrary value, the a-phase inverter nonlinearity voltages can be fitted by the PLI with several discrete points, as shown in Fig. 17.

In Fig. 17, (i_j, U_j) is the corresponding interpolation point, $j = 1, 2, \ldots, j_0$. By PLI, the fitted $u_{a\mathrm{err}}$ (i_a) can be expressed as (19), where M and N are the weights of the sampling voltage to the corresponding current in Fig. 17.

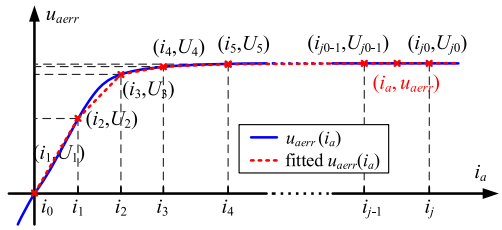

Fig. 17. PLI of a-phase inverter nonlinearity voltages along with the discrete interpolation points.

For simplicity, the d-axis coordinate transformation (15) is rewritten as

$$\begin{cases} u_{d\mathrm{err}}(i_d) = au_x(ai_d) + bu_x(bi_d) + cu_x(ci_d) \\ a = 2\cos(\theta_e)/3 \\ b = 2\cos(\theta_e - 2\pi/3)/3 \\ c = 2\cos(\theta_e + 2\pi/3)/3. \end{cases} \tag{A7}$$

Since $u_{d\mathrm{err}}$ (i_d) can be measured in the R_s identification process, (i_j, U_j) can be expressed by (i_{dj}, u_{dj}) which can be calculated by (A8).

M and N can be directly calculated by (19). The sampling points (i_j, U_j) can be gotten through RLS, which is shown as

$$\begin{aligned} \begin{bmatrix} u_d(i_0) \\ u_d(i_1) \\ \vdots \\ u_d(i_{j0}) \end{bmatrix} &= a \begin{bmatrix} M(ai_0) & N(ai_0) & & 0 \\ 0 & M(ai_1) & & 0 \\ 0 & 0 & \cdots & 0 \\ 0 & 0 & & N(ai_{j0}) \end{bmatrix} \begin{bmatrix} U_0 \\ U_1 \\ \vdots \\ U_{j0} \end{bmatrix} \\ &\quad + b \begin{bmatrix} M(bi_0) & N(bi_0) & & 0 \\ 0 & M(bi_1) & & 0 \\ 0 & 0 & \cdots & 0 \\ 0 & 0 & & N(bi_{j0}) \end{bmatrix} \begin{bmatrix} U_0 \\ U_1 \\ \vdots \\ U_{j0} \end{bmatrix} \\ &\quad + c \begin{bmatrix} M(ci_0) & N(ci_0) & & 0 \\ 0 & M(ci_1) & & 0 \\ 0 & 0 & \cdots & 0 \\ 0 & 0 & & N(ci_{j0}) \end{bmatrix} \begin{bmatrix} U_0 \\ U_1 \\ \vdots \\ U_{j0} \end{bmatrix} \\ &= [M, N]^{j_0 \times j_0} \begin{bmatrix} U_0 \\ U_1 \\ \vdots \\ U_{j0} \end{bmatrix}. \end{aligned} \tag{A8}$$

$$\begin{cases} \boldsymbol{e} = \boldsymbol{y} - \boldsymbol{\lambda}^T \boldsymbol{\rho} \\ \boldsymbol{\lambda}^T = [M, N]^{j_0 \times j_0} \\ \boldsymbol{y}^T = [u_d(i_0) u_d(i_1) \cdots u_d(i_{j0})] \\ \boldsymbol{\rho}^T = [U_0 U_1 U_2 U_3 \cdots U_{j0}] \end{cases} \tag{A9}$$

Finally, (19) can be obtained by the PLI in Fig. 17. In order to improve the fitting accuracy of $u_{a\mathrm{err}}$ (i_a), the number of interpolation points can be increased, especially in the nonlinear region at small current.

REFERENCES

[1] M. Slunjski, O. Stiscia, M. Jones, and E. Levi, "General torque enhancement approach for a nine-phase surface PMSM with built-in fault tolerance," *IEEE Trans. Ind. Electron.*, vol. 68, no. 8, pp. 6412–6423, Aug. 2021.

[2] G. Wang, R. Liu, N. Zhao, D. Ding, and D. Xu, "Enhanced linear ADRC strategy for HF pulse voltage signal injection-based sensorless IPMSM drives," *IEEE Trans. Power Electron.*, vol. 34, no. 1, pp. 514–525, Jan. 2019.

[3] G. Wang, R. Yang, and D. Xu, "DSP-based control of sensorless IPMSM drives for wide-speed-range operation," *IEEE Trans. Ind. Electron.*, vol. 60, no. 2, pp. 720–727, Feb. 2013.

[4] G. Zhang, G. Wang, D. Xu, and N. Zhao, "ADALINE-network-based PLL for position sensorless interior permanent magnet synchronous motor drives," *IEEE Trans. Power Electron.*, vol. 31, no. 2, pp. 1450–1460, Feb. 2016.

[5] P. Liang, F. Chai, Y. Li, and Y. Pei, "Analytical prediction of magnetic field distribution in spoke-type permanent-magnet synchronous machines accounting for bridge saturation and magnet shape," *IEEE Trans. Ind. Electron.*, vol. 64, no. 5, pp. 3479–3488, May 2017.

[6] F. Chai, L. Gan, and Y. Yu, "Magnetic field analysis of an iron-cored tiered type permanent magnet spherical motor using modified dynamic reluctance mesh method," *IEEE Trans. Ind. Electron.*, vol. 67, no. 8, pp. 6742–6751, Aug. 2020.

[7] C. Gong, Y. Hu, J. Gao, Y. Wang, and L. Yan, "An improved delay-suppressed sliding-mode observer for sensorless vector-controlled PMSM," *IEEE Trans. Ind. Electron.*, vol. 67, no. 7, pp. 5913–5923, Jul. 2020.

[8] S. Rubino, O. Dordevic, R. Bojoi, and E. Levi, "Modular vector control of multi-three-phase permanent magnet synchronous motors," *IEEE Trans. Ind. Electron.*, to be published, doi: 10.1109/TIE.2020.3026271.

[9] S. A. Odhano, P. Pescetto, H. A. A. Awan, M. Hinkkanen, G. Pellegrino, and R. Bojoi, "Parameter identification and self-commissioning in AC motor drives: A technology status review," *IEEE Trans. Power Electron.*, vol. 34, no. 4, pp. 3603–3614, Apr. 2019.

[10] M. S. Rafaq and J. Jung, "A comprehensive review of state-of-the-art parameter estimation techniques for permanent magnet synchronous motors in wide speed range," *IEEE Trans. Ind. Inform.*, vol. 16, no. 7, pp. 4747–4758, Jul. 2020.

[11] L. Peretti, P. Sandulescu, and G. Zanuso, "Self-commissioning of flux linkage curves of synchronous reluctance machines in quasi-standstill condition," *IET Power Appl.*, vol. 9, no. 9, pp. 642–651, Nov. 2015.

[12] N. Bedetti, S. Calligaro, and R. Petrella, "Stand-still self-identification of flux characteristics for synchronous reluctance machines using novel saturation approximating function and multiple linear regression," *IEEE Trans. Ind. Appl.*, vol. 52, no. 4, pp. 3083–3092, Jul./Aug. 2016.

[13] P. Pescetto and G. Pellegrino, "Automatic tuning for sensorless commissioning of synchronous reluctance machines augmented with high-frequency voltage injection," *IEEE Trans. Ind. Appl.*, vol. 54, no. 5, pp. 4485–4493, Sep./Oct. 2018.

[14] X. Wu, X. Fu, M. Lin, and L. Jia, "Offline inductance identification of IPMSM with sequence-pulse injection," *IEEE Trans. Ind. Inform.*, vol. 15, no. 11, pp. 6127–6135, Nov. 2019.

[15] J. Zhou, K. Huang, S. Huang, S. Liu, H. Zhao, and M. Shen, "Inductance parameter identification method of permanent magnet synchronous motor based on the HF rotating square wave voltage injection," in *Proc. 22nd Int. Conf. Electr. Mach. Syst.*, 2019, pp. 1–4.

[16] F. Erturk and B. Akin, "Spatial inductance estimation for current loop auto-tuning in IPMSM self-commissioning," *IEEE Trans. Ind. Electron.*, vol. 67, no. 5, pp. 3911–3920, May 2020.

[17] Q. Wang, G. Wang, N. Zhao, G. Zhang, Q. Cui, and D. Xu, "An impedance model-based multiparameter identification method of PMSM for both offline and online conditions," *IEEE Trans. Power Electron.*, vol. 36, no. 1, pp. 727–738, Jan. 2021.

[18] T. Liu, C. Wang, Y. Hu, Z. Ye, C. Zhong, and G. Griepentrog, "Offline inductance identification of PMSM using high frequency current signal injection," in *Proc. 22nd Int. Conf. Electr. Mach. Syst.*, 2019, pp. 1–8.

[19] S. Nadarajan, S. K. Panda, B. Bhangu, and A. K. Gupta, "Online model-based condition monitoring for brushless wound-field synchronous generator to detect and diagnose stator windings turn-to-turn shorts using extended Kalman filter," *IEEE Trans. Ind. Electron.*, vol. 63, no. 5, pp. 3228–3241, May 2016.

[20] X. Wang, Z. Wang, Z. Xu, M. Cheng, W. Wang, and Y. Hu, "Comprehensive diagnosis and tolerance strategies for electrical faults and sensor faults in dual three-phase PMSM drives," *IEEE Trans. Power Electron.*, vol. 34, no. 7, pp. 6669–6684, Jul. 2019.

[21] T. Strinić and W. Gruber, "Self-commissioning of permanent magnet synchronous machines by considering nonlinearities of the voltage source inverter," in *Proc. 45th Annu. Conf. IEEE Ind. Electron. Soc.*, 2019, pp. 1320–1326.

[22] F. Stella, A. Yousefi-Talouki, S. Odhano, G. Pellegrino, and P. Zanchetta, "An accurate self-commissioning technique for matrix converters applied to sensorless control of synchronous reluctance motor drives," *IEEE J. Emerg. Sel. Top. Power Electron.*, vol. 7, no. 2, pp. 1342–1351, Jun. 2019.

[23] X. Wu, M. Lin, P. Wang, L. Jia, and X. Fu, "Off-line stator resistance identification for PMSM with pulse signal injection avoiding the dead-time effect," in *Proc. 22nd Int. Conf. Electr. Mach. Syst.*, 2019, pp. 1–5.

[24] Q. Wang, G. Zhang, G. Wang, C. Li, and D. Xu, "Offline parameter self-learning method for general-purpose PMSM drives with estimation error compensation," *IEEE Trans. Power Electron.*, vol. 34, no. 11, pp. 11103–11115, Nov. 2019.

[25] G. Wang *et al.*, "Self-commissioning of permanent magnet synchronous machine drives at standstill considering inverter nonlinearities," *IEEE Trans. Power Electron.*, vol. 29, no. 12, pp. 6615–6627, Dec. 2014.

[26] Y. Wang, W. Xie, X. Wang, and D. Gerling, "A precise voltage distortion compensation strategy for voltage source inverters," *IEEE Trans. Ind. Electron.*, vol. 65, no. 1, pp. 59–66, Jan. 2018.

[27] S. M. Seyyedzadeh and A. Shoulaie, "Accurate modeling of the nonlinear characteristic of a voltage source inverter for better performance in near zero currents," *IEEE Trans. Ind. Electron.*, vol. 66, no. 1, pp. 71–78, Jan. 2019.

[28] Z. Liu, H. Wei, Q. Zhong, K. Liu, X. Xiao, and L. Wu, "Parameter estimation for VSI-Fed PMSM based on a dynamic PSO with learning strategies," *IEEE Trans. Power Electron.*, vol. 32, no. 4, pp. 3154–3165, Apr. 2017.

[29] G. Feng, C. Lai, K. Mukherjee, and N. C. Kar, "Current injection-based online parameter and VSI nonlinearity estimation for PMSM drives using current and voltage DC components," *IEEE Trans. Power Electron.*, vol. 2, no. 2, pp. 119–128, Jun. 2016.

[30] N. Bedetti, S. Calligaro, and R. Petrella, "Self-commissioning of inverter dead-time compensation by multiple linear regression based on a physical model," *IEEE Trans. Ind. Appl.*, vol. 51, no. 5, pp. 3954–3964, Sep./Oct. 2015.

[31] P. Sun, C. Gong, X. Du, Q. Luo, H. Wang, and L. Zhou, "Online condition monitoring for both IGBT module and DC-link capacitor of power converter based on short-circuit current simultaneously," *IEEE Trans. Ind. Electron.*, vol. 64, no. 5, pp. 3662–3671, May 2017.

[32] G. Wang, Y. Wang, J. Qi, R. Ni, W. Chen, and D. Xu, "Offline inductance identification of PMSM with adaptive inverter nonlinearity compensation," in *Proc. 9th Int. Conf. Power Electron. ECCE Asia*, 2015, pp. 2438–2444.

Qiwei Wang received the B.S. and M.S. degrees in electrical engineering in 2015 and 2017, respectively, from the Harbin Institute of Technology, Harbin, China, where he is currently working toward the Ph.D. degree in power electronics and electrical drives at the School of Electrical Engineering and Automation.

His current research interests include parameter identification technique and PMSM position sensorless control.

Nannan Zhao (Member, IEEE) received the B.S. and M.S. degrees in control science and engineering and the Ph.D. degree in electrical engineering from Harbin Institute of Technology, Harbin, China, in 2013, 2015, and 2019, respectively.

He is currently a Postdoctoral Fellow and a Lecturer with the School of Electrical Engineering and Automation, Harbin Institute of Technology. His current research interests include advanced control of permanent magnet synchronous motor drives and position sensorless control of ac motors.

Dr. Zhao is currently supported by Postdoctoral Innovative Talent Support Program of China.

Gaolin Wang (Senior Member, IEEE) received the B.S., M.S., and Ph.D. degrees in electrical engineering from the Harbin Institute of Technology, Harbin, China, in 2002, 2004, and 2008, respectively.

He joined as a Lecturer with the Department of Electrical Engineering, Harbin Institute of Technology, in 2009, where he has been a Full Professor of Electrical Engineering since 2014. From 2009 to 2012, he was a Postdoctoral Fellow with Shanghai Step Electric Corporation, China, where he was involved in the traction machine control for direct-drive elevators. He has authored more than 60 technical papers published in journals and conference proceedings. He is the holder of ten Chinese patents. His current major research interests include permanent magnet synchronous motor drives, high-performance direct-drive for traction systems, position sensorless control of ac motors, efficiency optimization control of PMSM, and digital control of power converters.

Dr. Wang serves as a Guest Editor for IEEE TRANSACTIONS ON INDUSTRIAL ELECTRONICS, an Associate Editor for *IEEE Access*, *IET Electric Power Applications*, and *Journal of Power Electronics*.

Shouhua Zhao received the Ph.D. degree in electrical engineering from Zhejiang University, Hangzhou, China, in 2015.

He is currently a Senior Engineer of motor control with CRRC Zhuzhou Motor Co., Ltd., Zhuzhou, China. His current research interests include parameter identification technology and sensorless position control of permanent magnet synchronous motor.

Zhixue Chen received the B.S. degree in electrical engineering from Shandong University of Science and Technology, Qingdao, China, in 2012, and the M.S. degree in electrical engineering from Shenyang University of Technology, Shenyang, China, in 2016.

He is currently a Motor Control Engineer with CRRC Zhuzhou Electric Machinery Co., Ltd., Zhuzhou, China. His current research interests include parameter identification technology and sensorless position control of permanent magnet synchronous motors.

Guoqiang Zhang (Member, IEEE) received the B.S. degree in electrical engineering from Harbin Engineering University, Harbin, China, in 2011, and the M.S. and Ph.D. degrees in electrical engineering from Harbin Institute of Technology, Harbin, China, in 2013 and 2017, respectively.

He is currently a Postdoctoral Fellow and a Lecturer with the Department of Electrical Engineering, Harbin Institute of Technology. His current research interests include parameter identification technique and control of electrical drives, with main focus on sensorless field-oriented control of interior permanent magnet synchronous machines.

Dr. Zhang serves as an Associate Editor for *Journal of Power Electronics*.

Dianguo Xu (Fellow, IEEE) received the B.S. degree in control engineering from the Harbin Engineering University, Harbin, China, in 1982, and the M.S. and Ph.D. degrees in electrical engineering from the Harbin Institute of Technology (HIT), Harbin, China, in 1984 and 1989, respectively.

He joined the Department of Electrical Engineering, HIT, as an Assistant Professor, in 1984. Since 1994, he has been a Professor with the Department of Electrical Engineering, HIT. From 2000 to 2010, he was the Dean of the School of Electrical Engineering and Automation, HIT, and was the Assistant President from 2010 to 2014. He is currently the Vice President of the HIT. He has authored or coauthored more than 600 technical papers. His research interests include renewable energy generation technology, power quality mitigation, sensorless vector controlled motor drives, and high-performance PMSM servo system.

Dr. Xu is an Associate Editor for the IEEE TRANSACTIONS ON INDUSTRIAL ELECTRONICS and the *IEEE Journal of Emerging and Selected Topics in Power Electronics*. He serves as the Chairman of the IEEE Harbin Section.